Techno-Economic Modeling and Optimization of Flexible Geothermal Operations Coupled with Energy Storage

Mohammad J. Aljubran, Oleg Volkov and Roland N. Horne

Stanford Geothermal Program, Stanford, California 94305, United States

aljubrmj@stanford.edu

ABSTRACT

Dispatchable energy resources are key for a reliable power supply. Whereas in the past the development of fossil fuel resources has dominated the supply for dispatchable capacity, this trend is slowing down due to the growing climate change concerns and the transition to renewable resources. Geothermal energy has always been an economic resource for district heating and baseload power. With the decline of fossil fuel plants, geothermal facilities have been expanding beyond baseload to supply flexible heat and electricity. There has been a limited number of studies that investigate the feasibility of flexibly dispatching geothermal power to the wholesale power market in the absence of fixed-price power purchase agreements (PPAs). This study performed techno-economic modeling and optimization of flexible geothermal power dispatch when coupled with thermal energy or Lithium-ion battery storage.

We developed a techno-economic model to optimize system design (e.g., power plant, thermal tank, and Lithium-ion battery storage capacities) and dispatch schedule (e.g., turbine bypass, and dis/charging thermal tank and Lithium-ion battery) with the goal of maximizing the project net present value (NPV). Costs included capital and operational expenditure for upstream reservoir development, power plant, and storage facilities, while revenue streams included wholesale power markets, capacity value, and renewable energy certificates (RECs). We posed the problem as a mixed integer, multi-objective setting and solved it using the Reference-Point Based Non-Dominated Sorting Genetic Algorithm (R-NSGA-II) which offers robust means of efficiently finding the global optima.

We examined a 220° C, liquid-dominated geothermal resource developed with 6 producers and 6 injectors developed with a subcritical Organic Rankine Cycle power plant. We used a conceptual subsurface model to simulate temperature decline over time alongside correlations to estimate power plant efficiency under different operating conditions. Economics was based on 30-year forecasts of the California power markets. Results indicate that participating in the free market with a 66 MW power plant without added storage facilities results in profits equivalent to signing a PPA with 82.4 $/MWh fixed price. While adding thermal storage was found to be suboptimal, Lithium-ion battery storage results in a more profitable system equivalent to signing a PPA with nearly 105 $/MWh.

This work shows that flexible geothermal dispatch is techno-economically feasible from the perspective of the developer. Flexible portfolios are also desired by system operators, especially in decarbonized grids. Additionally, our results indicate that geothermal systems could be developed economically for power generation even in the absence of PPAs.

1. INTRODUCTION

The California net-zero carbon economy has been dependent on the rapid growth of solar and wind electricity, as well as electrification of transportation and heating. However, the increasing reliance on weather-dependent renewables can raise grid reliability challenges which mandate careful resource planning. This raises the need for "clean firm power": carbon-free power resources that are always available for as long as needed. Diversity of resources across dispatch capabilities is also desirable and found to further reduce the costs of full grid decarbonization (Long et al. 2021). Generally, a renewable resource is more appealing when it can integrate cost-effectively into the energy mix and shift its power output to span diverse forms of dispatch, e.g., baseload, hourly, daily, and seasonal.

Geothermal energy provides clean firm power, which has been viewed historically as a baseload or "always-on" resource with high-capacity factors (CF). Given the high upfront risk and capital expenditure, geothermal power operators typically operate under power purchase agreements (PPAs). However, the high penetration of intermittent resources caused an increase in the value of dispatchable geothermal generation that would fill in the diurnal and seasonal gaps. Under the Grid Modernization Initiative launched by the U.S. Department of Energy (DOE), the Geothermal Technologies Office invested in the Beyond Batteries initiative which aims to integrate geothermal energy into a flexible and controllable resource through underground storage (Dobson et al. 2020). In the 2021 U.S. Geothermal Power Production and District Heating Market Report, the National Renewable Energy Laboratory (NREL) identified dispatchable geothermal energy as one of the top ten emerging geothermal technologies (Robins et al. 2021). Hence, there is a need for further techno-economic analysis to evaluate the economics and requirements of flexible geothermal operations for future decarbonized electricity grids. This paper performed techno-economic optimization of flexible geothermal power dispatch when coupled with thermal energy or Lithium-ion battery storage.

2. LITERATURE REVIEW

Due to the relatively recent interest in dispatchable geothermal resources, we have found only limited studies and field implementations in the direction of flexible geothermal operations. We reviewed these implementations to develop an understanding of what options are available to achieve dispatchable geothermal operations.

Globally, researchers and engineers across different geothermal institutes and organizations have followed different approaches to achieve dispatchable geothermal operations. Recognizing that economic feasibility is essential, technical variability across methods is mainly governed by the geothermal reservoir and power plant configuration. Conventional geothermal reservoirs are generally either liquid-dominated or vapor-dominated, depending on which phase/s is mobile in the subsurface porous media. It is important to note that most global geothermal resources are liquid-dominated. Other nonconventional geothermal resources also exist, such as enhanced geothermal systems (EGS), but they are less common and under ongoing research and development (Olasolo et al. 2016). Geothermal power plants are commonly classified into three main categories: dry steam, flash steam, and binary cycle (Augustine et al. 2019). Although they are less common, other power plant configurations also exist, e.g., multiflash, combined cycle, amongst others (Dipippo 2012). Optimal reservoir management and production engineering are governed by the type of the associated geothermal resource. Also, each power plant configuration is characterized with different operating requirements and power generation efficiencies. Hence, in addition to the economic viability, it is inevitable to consider operational challenges in pursuit of dispatchable operations.

Based on our literature review of the studies and implementations of dispatchable geothermal energy, we classified such flexible operations into four main categories: (1) wellhead throttling, (2) steam vent-off, (3) turbine bypass, and (4) storage. A recent study evaluated the impact of wellhead throttling in vapor- and liquid-dominated geothermal reservoirs using data from The Geysers and Casa Diablo, respectively (Rutqvist et al. 2020). They found wellhead throttling to be more feasible in liquid-dominated compared to steam-dominated systems. Steam vent-off has been commonly used across fields (Minson et al. 1985; Hardarson et al. 2018) given its ease, yet it is extremely suboptimal. Meanwhile, turbine bypass is another option that has been used for curtailment in fields such as The Geysers and Puna geothermal fields (Dobson et al. 2020; Nordquist et al. 2013). Lastly, storage is a newly emerging approach for flexible geothermal operations with limited pilot design and evaluation of surface thermal energy (Garabetian 2021; Petursdottir et al. 2020; TWI 2020) and underground storage in EGS (Ricks et al. 2022).

3. PROBLEM FORMULATION

Since the start of the 21st century, most newly built geothermal power plants in the US have been binary as they are suitable for power generation from more common low-enthalpy resources and provide a closed system on the surface with zero emissions (Linga 2019). Therefore, we considered a binary power plant in our problem definition, although it would be straightforward to modify it for flash or combined cycle power plants. As seen in Figure 1, produced geofluid flows from one or more producer wells at variable mass flow rates, passes through a heat exchanger (e.g., vaporizer and preheater train) to boil a binary working fluid, and is reinjected at one or more injector wells with variable mass flow rates. The boiling binary working fluid spins a turbine to generate power and then runs through a dry condenser before reentering the heat exchanger train. We considered three means for flexible generation: (1) power plant bypass, (2) thermal energy storage (TES) tank, and (3) Lithium-ion battery storage. Whereas TES units can be functional for the typical geothermal power lifetime of 30 years, Lithium-ion battery storage will have to be replaced once given its typically shorter lifetime of 15-20 years. We are particularly interested in projects that are fully or partially financed in the absence of PPAs, where revenue is earned through trading in the free market as managed by an independent system operator (ISO). In this work, we considered three revenue streams: wholesale market based on real-time (RT) locational marginal prices (LMP), capacity market, and renewable energy certificates (RECs) market.
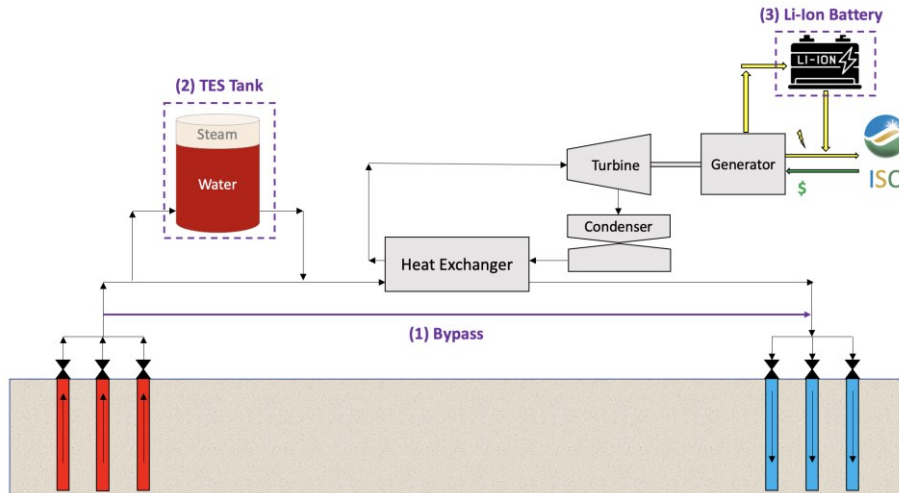

Figure 1: Simplified drawing of a geothermal resource developed with producers and injectors, and a binary power plant. Additionally, this setup incorporates three means for flexible geothermal power operations (1) power plant bypass line, (2) TES tank, and (3) Lithium-ion battery. Revenue is acquired from trading in the free market through ISO, with no PPA in place.

We categorized the problem parameters into fixed variables, state variables, and decision variables. Fixed variables ($\boldsymbol{f}$) include the initial development design, i.e., subsurface geothermal model, number of producers (N_{prd}), number of injectors (N_{inj}), wellbore configurations, nameplate power plant capacity (PPC), capacity factor (CF), bypass piping, TES tank design, and Lithium-ion battery design. Whereas we fixed most of these variables, we optimized for PPC, TES tank volumetric capacity, and Lithium-ion battery power and energy capacities while simultaneously solving for the respectively optimal dispatch schedule. State variables ($\boldsymbol{s}$) vary over time (t) and must be computed for each timestep Δt. The state variables can be divided into three categories: upstream, downstream, and electricity market. Upstream state variables are associated with the reservoir and wellbore conditions, i.e., reservoir pressure (P_t^r) and temperature (T_t^r), and producer wellhead temperature (T_t^{prd}). Downstream state variables relate to the power plant output, i.e. ambient temperature (T_t^{amb}), injection water temperature (T_t^{inj}), geofluid consumption efficiency (η_t^{pp}), tank heat loss rate ($\dot{Q}_t^{HL}$) and steam quality (x_t) at thermodynamic equilibrium, battery state of charge (SOC), and operational limits of ramp up/down rate (UC_t^{ramp}). State variables also involve the state of electricity market, i.e., real-time (RT) market prices (p_t^{RT}), capacity value (p_t^{Cap}), RECs value (p_t^{REC}), and battery effective load carrying capacity ($ELCC_t^{bat}$). Lastly, decision variables ($\boldsymbol{x}$) are quantities determined by the optimizer with the objective of maximizing the economic value of the flexible geothermal system operations. Some decision variables are static, i.e., tank volumetric capacity (V_{tank}), and primary and replacement battery power capacities (BC^{bat_1}, BC^{bat_2}) and durations (BD^{bat_1}, BD^{bat_2}). Other decision quantities are temporal, i.e., turbine bypass mass flow rate ($\dot{m}_t^{bypass}$), producer well mass flow rates ($\dot{m}_t^{prd}$), injector well mass flow rates ($\dot{m}_t^{inj}$), TES charge ($\dot{m}_t^{charge}$) and discharge ($\dot{m}_t^{discharge}$) mass flow rates, and battery charge ($\dot{p}_t^{charge}$) and discharge ($\dot{p}_t^{discharge}$) power.

3.1 Financial Parameters

To evaluate the profitability of flexible generation scenarios, we should also define economic parameters. With geothermal power plant lifetime of N_l^{pp} years and inflated nominal discount rate d, the objective is to maximize the net present value (NPV) defined as the sum of discounted annual profits, seen in Eqs. 1-6. For a given year n, annual profits are defined as the difference between the annual revenue (R_n) and annual cost (C_n). The latter is calculated as the sum of the annual short-run marginal cost ($SRMC_n$) of total annual generation (G_n), and fixed cost of capacity ($FCOC_n$) which is constant over years. Since geothermal power does not involve carbon emission and fuel costs, $SRMC_n$ is equal to the variable operation and maintenance cost (VOM_n) minus production tax credit (PTC_n). Meanwhile, $FCOC_n$ is equal to the sum of the levelized cost of capacity ($LCOC_n$) and annual fixed operation and maintenance cost (FOM_n) minus investment tax credit (ITC_n). We used the cost recovery factor (CRF) to calculate $LCOC_n$ for overnight capacity cost C_{cap} including surface storage tank cost. As seen in Eq. 7, we can also calculate the levelized cost of energy ($LCOE$) based on the project annual expenditure and power generation. Meanwhile, R_n is calculated as the revenue from the RT, capacity, and RECs markets based on the generation schedule, as seen in Eq. 8, where $G_{\{t,i\}}^{RT} = G_{\{t,i\}}$, since the RT market is treated as the sole revenue stream to wholesale markets. Note that $effective\ PPC$ accounts for reservoir depletion, while $G_{\{t,i\}}$ is a function of the flexible dispatch schedule.

$$NPV = \sum_{n=0}^{N_l^{pp}} \frac{R_n - C_n}{(1+d)^n} \qquad\qquad \text{Eq 1}$$

$$C_n = SRMC_n \cdot G_n + FCOC_n \cdot PPC \qquad\qquad \text{Eq 2}$$

$$SRMC_n = VOM_n - PTC_n \qquad\qquad \text{Eq 3}$$

$$FCOC_n = LCOC_n + FOM_n - ITC_n \qquad\qquad \text{Eq 4}$$

$$LCOC_n = CRF \cdot C_{cap} \qquad\qquad \text{Eq 5}$$

$$CRF = \frac{d \cdot (1+d)^{N_l^{pp}}}{(1+d)^{N_l^{pp}} - 1} \qquad\qquad \text{Eq 6}$$

$$LCOE = \frac{\sum_{n=0}^{N_l^{pp}} \frac{C_n}{(1+d)^n}}{\sum_{n=0}^{N_l^{pp}} \frac{G_n}{(1+d)^n}} \qquad\qquad \text{Eq 7}$$

$$R_n = \underbrace{\left(effective\ PPC \cdot ELCC_n^{pp} + BC_n^{bat} \cdot ELCC_n^{bat}\right) \cdot p_n^{Cap}}_{capacity\ revenue} + \underbrace{\sum_t^{8760} \sum_i G_{\{t,i\}}^{RT} \cdot \left(p_{\{t,i\}}^{RT} + p_{\{t,i\}}^{RECs}\right)}_{RT\ and\ RECs\ revenue} \qquad\qquad \text{Eq 8}$$

3.2 Physical Parameters

This problem requires the definition of a subsurface model to simulate temperature decline, a binary power plant model to simulate the geofluid consumption and reinjection fluid conditions, and a thermal storage model to simulate heat losses and thermodynamic equilibrium across the surface storage tank. Whereas we adopted conceptual models and correlations to simulate temperature decline and binary power plant efficiency, we built heat loss and thermodynamic equilibria models to simulate thermal storage.

Because this problem of flexible generation does not involve wellhead throttling, then producer and injector mass flow rates $\dot{m}_t^{prd}$ and $\dot{m}_t^{inj}$, respectively, are held constant. Therefore, we can assume a percentage thermal drawdown model, where temperature decline based on an initial reservoir temperature and fixed decline rate ρ across timesteps (Beckers and McCabe 2019). Neglecting wellbore heat losses,

Aljubran et al.

Eq. 9 describes the producer wellhead temperature T_t^{prd} over time which is assumed to be identical across all producer wells. In this work, we assume $\rho = 0.005$, reservoir true vertical depth of 4 km, surface temperature of $20°$ C, and geothermal gradient of $50\ °C/km$; hence, an initial reservoir temperature of $T_0^r = 220°\ C$.

$$T_{t+1}^{prd} = (1 - \rho)\ T_t^{prd} \hspace{6cm} \text{Eq 9}$$

In modeling power plant thermodynamics, we considered a subcritical Organic Rankine Cycle (ORC) power plant modeled using correlations originally developed for GEOPHIRES, a geothermal project economics module produced by NREL scientists (Beckers and McCabe 2019). This correlation predicts the power plant geofluid consumption η_t^{pp} and reinjection water temperature T_t^{inj} for different combinations of wellhead temperature T_t^{prd} and ambient temperature T_t^{amb}.

Tank heat losses at each timestep Δt were computed based on heat transfer principles of conduction, convection, and radiation (Orsini et al. 2021; Lienhard and John 2005; Bergman et al. 2011). As seen in Figure 2, we considered an insulated steel tank of height H, diameter D, top/bottom surface area A^{roof}, sides surface area A^{sides}, steel inner and outer radii $r^{\{in,st\}}$ and $r^{\{out,st\}}$, insulation inner and outer radii $r^{\{in,ins\}}$ and $r^{\{out,ins\}}$, steel wall thickness L^{st}, and insulation wall thickness L^{ins}. The tank is assumed to have steady material temperature for small infinitesimally timestep Δt. At each Δt, we perform two steps: (1) heat transfer, and (2) thermodynamic equilibrium calculations.
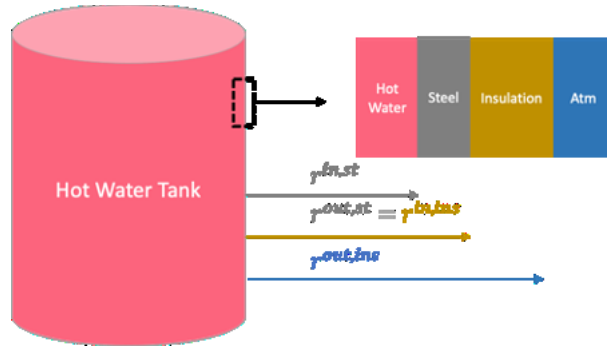

Figure 2: Insulated steel thermal storage tank, where heat losses are considered across the side and top/bottom walls.

We first addressed the heat loss calculations using heat transfer principles. As seen in Eqs. 10-16, the conductive heat loss rate across the steel wall $\dot{Q}^{cond,st}$ is then equal to the conductive heat loss rate across the insulation wall $\dot{Q}^{cond,ins}$, and also equal to the total convective $\dot{Q}^{conv}$ and radiative $\dot{Q}^{rad}$ heat loss rates to the atmosphere (Note that we omit subscript t for convenience). Conductive heat losses are driven by the thermal conductivity coefficients k^{st} and k^{ins}, and include those at the sides $\dot{Q}^{cond,i,sides}$, top $\dot{Q}^{cond,i,top}$, and bottom $\dot{Q}^{cond,i,btm}\ \forall\ i \in \{st,ins\}$. Also, convective $\dot{Q}^{conv}$ and radiative $\dot{Q}^{rad}$ heat loss rates are calculated as functions of T^{amb} and A^{sides} using the convective heat transfer coefficient u and the Stefan-Boltzmann constant σ, respectively. This is a system of two equations and two variables which we solve analytically to find $T^{st}(r^{out,st})$, $T^{ins}(r^{out,ins})$, and $\dot{Q}^{cond,st}$. Using the system heat loss rate, i.e. $\dot{Q}^{cond,st}$, we can finally calculate the tank temperature drop ΔT^{tank} for a timestep Δt using the water and steam isobaric specific heat capacities and mass inside the tank, i.e. $c^w, c^s, m^{tank,w}$ and $m^{tank,s}$, respectively.

$$\dot{Q}^{cond,st} = \dot{Q}^{cond,ins} = \dot{Q}^{conv} + \dot{Q}^{rad} \hspace{5cm} \text{Eq 10}$$

$$\dot{Q}^{cond,i} = \dot{Q}^{cond,i,sides} + \dot{Q}^{cond,i,top} + \dot{Q}^{cond,i,btm} \hspace{3.5cm} \text{Eq 11}$$

$$\dot{Q}^{cond,i,sides} = \frac{2\pi H k^i [T^i(r^{in,i}) - T^i(r^{out,i})]}{\ln\frac{r^{out,i}}{r^{in,i}}} \hspace{1cm} \forall\ i \in \{st,ins\} \hspace{2cm} \text{Eq 12}$$

$$\dot{Q}^{cond,i,j} = \frac{A^{roof} k^i [T^i(r^{in,i}) - T^i(r^{out,i})]}{L^i} \hspace{0.7cm} \forall\ i \in \{st,ins\}\ \ and\ \ \forall\ j \in \{top,btm\} \hspace{0.5cm} \text{Eq 13}$$

$$\dot{Q}^{conv} = A^{sides} u\ [T^{ins}(r^{out,ins}) - T^{amb}] \hspace{4cm} \text{Eq 14}$$

$$\dot{Q}^{rad} = A^{sides} \sigma\ [\ T^{ins}(r^{out,ins})^4 - (T^{amb})^4] \hspace{3.5cm} \text{Eq 15}$$

$$\Delta T^{tank} = \frac{\dot{Q}^{cond,st} \cdot \Delta t}{c^w m^{tank,w} + c^s m^{tank,s}} \hspace{4.5cm} \text{Eq 16}$$

In modeling heat losses, we require knowledge of water and steam mass inside the tank at each timestep. Hence, we also need to run flash calculations to establish thermodynamic equilibrium, and account for energy and mass balance with respect to the tank. As seen in $(m_{t+\Delta t}^w h_{t+\Delta t}^w + m_{t+\Delta t}^s h_{t+\Delta t}^s) - (m_t^w h_t^w + m_t^s h_t^s) = (\dot{m}_t^{charge} h_t^{charge} - \dot{m}_t^{discharge} h_t^{discharge} - \dot{Q}^{cond,st}) \Delta t$ Eq 17, we use control volume around the tank over each timestep Δt and account for the enthalpy flow in/out of the tank, enthalpy accumulation, and heat losses. As seen in Eq. 18, we similarly formulate the mass balance around the storage tank. Given the tank volume V^{tank}, we must

also establish thermodynamic water-steam equilibrium after each timestep Δt by accounting for the two-phase specific volume v and steam quality x, seen in Eqs 19-20. Note that enthalpy h_t and specific volume v_t are implicitly estimated using steam tables (Holmgren 2006) as functions of T_t^{tank} which also changes over time. Finally, we solve for $m_{t+\Delta t}^w$, $m_{t+\Delta t}^s$, and $T_{t+\Delta t}^{tank}$. This is solved iteratively by minimizing the sum of squared residuals of the system equations (Virtanen et al. 2020; Garbow 1984).

$$(m_{t+\Delta t}^w\, h_{t+\Delta t}^w + m_{t+\Delta t}^s\, h_{t+\Delta t}^s) - (m_t^w\, h_t^w + m_t^s\, h_t^s) = \left(\dot{m}_t^{charge} h_t^{charge} - \dot{m}_t^{discharge} h_t^{discharge} - \dot{Q}_t^{cond,st}\right)\Delta t \qquad \text{Eq 17}$$

$$(m_{t+\Delta t}^w + m_{t+\Delta t}^s) - (m_t^w + m_t^s) = \left(\dot{m}_t^{charge} - \dot{m}_t^{discharge}\right)\Delta t \qquad \text{Eq 18}$$

$$v_{t+\Delta t}^{tank} = \frac{V^{tank}}{m_{t+\Delta t}^w + m_{t+\Delta t}^s} \qquad \text{Eq 19}$$

$$x_{t+\Delta t} = \frac{m_{t+\Delta t}^s}{m_{t+\Delta t}^w + m_{t+\Delta t}^s} = \frac{v_{t+\Delta t}^{tank} - v_{t+\Delta t}^w}{v_{t+\Delta t}^s + v_{t+\Delta t}^w} \qquad \text{Eq 20}$$

3.3 Optimization Algorithm

The objective is to maximize a profit function $f(\boldsymbol{x})$ by solving for the optimal static and temporal decision variables $\boldsymbol{x} = [\boldsymbol{x_{static}}, \boldsymbol{x_{temporal}}]$. Whereas $\boldsymbol{x_{static}}$ belongs to a low-dimensional space, $\boldsymbol{x_{temporal}}$ belongs to an infeasibly high-dimensional space where each temporal physical quantity is associated with a total number of timesteps $T = 30 \cdot 8{,}760 = 262{,}800$ timesteps. Therefore, we introduced a technique to reversibly reduce the space of $\boldsymbol{x_{temporal}}$ through optimizing a data-driven encoder-decoder transformation (Michalewicz and Fogel 2013).

As seen in Figure 3 and Eq. 21, considering a temporal quantity "i", we hypothesize that the corresponding optimal decision vector $\boldsymbol{x_{temporal,i}^*}$ can be expressed through a functional transformation $\mathcal{R}(\cdot; W_i)$, parametrized with W_i, of independent and known temporal state variables denoted by $\boldsymbol{p} \in \mathbb{R}^{T \times k}$. Note that k represents the number of those independent and known variables, which in this problem are $[p^{RT}, p^{Cap}, p^{REC}]$. The choice of $\mathcal{R}(\cdot; W_i)$ should be parametrizable in a low-dimensional space $\dim(W_i) \ll \dim(\boldsymbol{x_{temporal,i}})$, sufficiently expressive, and computationally inexpensive. As seen in Eqs. 22-23, because we are mapping temporal quantities with varying frequencies, we chose $\mathcal{R}$ as a sequence of parameter-free empirical mode decomposition (EMD_{d_1}) with d_1 modes where $EMD_{d_1}(\boldsymbol{p}) \in \mathbb{R}^{T \times (kd_1)}$, and a two-layer feedforward neural network parameterized with $\theta_i^{(1)} \in [-1,1]^{(kd_1) \times d_2}$ and $\theta_i^{(2)} \in [-1,1]^{d_2}$, where $k, d_1, d_2 \in \mathbb{N}$. Note that we also introduced rescaling and thresholding factors $\alpha_i, \beta_i \in \mathbb{R}$, respectively. Hence, the goal is to solve for $\boldsymbol{x_{static}^*}$ and W_i^* to find $\boldsymbol{x}^*$. In other words, we reduced the dimensionality for each temporal physical quantity to $d_2(kd_1 + 1) + 2 = \dim(W_i) \ll \dim(\boldsymbol{x_{temporal,i}}) = T = 262{,}800$. In this study, we chose $d_1 = d_2 = 5$ and $\boldsymbol{p} = [p^{RT}] \in \mathbb{R}^T$, hence $k = 1$, because the wholesale real-time market is the primary driver of the dispatch schedule in our settings. Note that we adopted the *PyEMD* implementation of EMD_{d_1} (Laszuk 2017).

$$\boldsymbol{x_{temporal,i}^*} \approx \mathcal{R}(\boldsymbol{p}; W_i^*) \qquad \text{Eq 21}$$

$$ReLU_\beta(y) = \begin{cases} y; & y > \beta \\ 0; & y \leq \beta \end{cases} \qquad \text{Eq 22}$$

$$\boldsymbol{x_{temporal,i}} = \mathcal{R}(\boldsymbol{p}; W_i) = \alpha_i \cdot ReLU_{\beta_i}\left(ReLU_0\left(EMD_{d_1}(\boldsymbol{p}) \cdot \theta_i^{(1)}\right) \cdot \theta_i^{(2)}\right) \qquad \text{Eq 23}$$
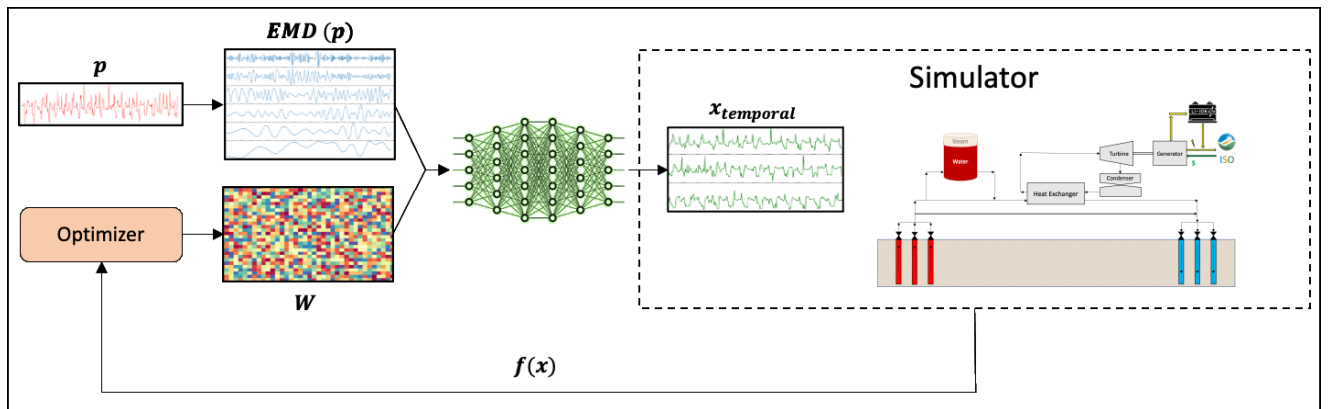

Figure 3: Optimization framework showing the data-driven encoder-decoder transformation (EMD and neural network) as means of dimensionality reduction.

Beyond decision variables, we also consider bound, equality, and inequality constraints on physical quantities to satisfy conservation laws, but we do not constrain sales to the power market. To ease the optimization problem, we satisfy equality and inequality constraints of

physical constraints (e.g., TES tank volumetric limits, battery dis/charge rates, turbine capacity, etc.) within the integrated flexible geothermal system simulation module. Hence, aside from bound constraints, this becomes an unconstrained optimization problem. We used genetic algorithms as gradient-free global optimization solvers (Mitchell 1998). However, when solely optimizing for NPV, finding the global optima in a highly nonlinear setting with multiple interdependent decision variables can be difficult. During the first few optimization iterations, the dispatch schedule $x_{temporal}$ is far from optimal; hence, the optimizer tended to dismiss the installation of the costly TES and battery storage facilities and simply operates in baseload mode, which could be a local optimum. This problem persisted in single-objective optimization even with more significant and frequent mutation transformations because $\dim(x_{static}) \ll \dim(x_{temporal})$. As a solution, we posed this problem as a dual-objective optimization, where we optimize over NPV and $Net\ Income$. This encourages exploration of various system designs despite high upfront cost, which often involves storage. Additionally, noting that capital expenditure $CAPEX = Net\ Income - NPV$, this approach allows for systematically exploring the NPV versus $CAPEX$ Pareto front during optimization. Finally, we solved this mixed-integer, dual-objective optimization problem using the Reference-Point Based Non-Dominated Sorting Genetic Algorithm (R-NSGA-II) which provides robust means of efficiently finding global optima (Deb and Sundar 2006). We adopted the *pymoo* implementation of R-NSGA-II (Blank and Deb 2020).

4. CASE STUDY

To evaluate the techno-economics of a 30-year flexible geothermal system coupled with storage in California, we mainly require forecasts for the wholesale, capacity and REC markets, and battery capital and operational expenses. We used a publicly accessible avoided cost calculator (ACC) developed by Energy and Environmental Economics, Inc. (E3 2022) which spans 2021-2050 for the California trading hub NP15. To conduct an evaluation with respect to potential future investments in geothermal and storage systems, we considered a project launched in 2025 with a 30-year financial lifetime. To fully span the project lifetime of 2025-2055, we linearly extrapolated the 2022 E3 ACC market forecasts based on yearly growth/decline to cover the period of 2050-2055. As it is atypical to forecast RECs market value, it can be substituted for the carbon cap and trade value which is forecasted in the 2022 E3 ACC calculator. As seen in Figure 4, RT LMPs and REC values both depict a "duck curve" behavior with varying trends over years due to the forecasted expansion in solar and storage capacity. Figure 5 demonstrates the respective forecasts for the capacity market and battery ELCC. We note that capacity value is relatively high in the first few years and declines continuously to zero. This is because the 2022 E3 ACC model bases capacity value on battery capacity expansion in California, which is forecasted to increase significantly resulting in diminishing capacity values in the presence of wholesale and REC markets depicted in Figure 4. Lithium-ion battery ELCC is forecasted to also diminish as battery power capacity increases in the California power system. Note that battery ELCC in today's California market is about 90%.
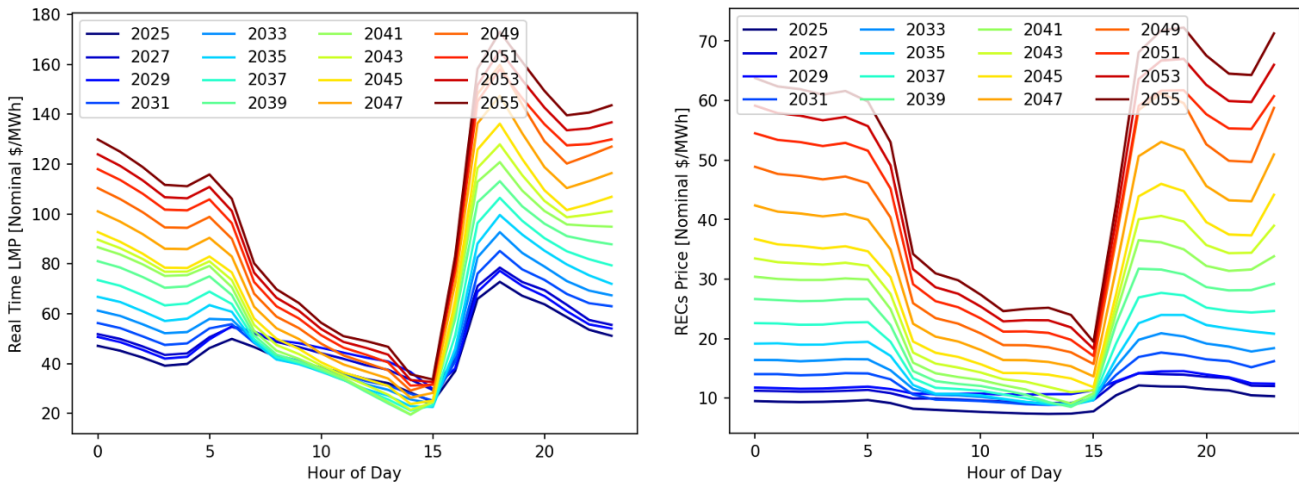

Figure 4: Annual average hourly price forecasts for the RT (left) and REC (right) markets based on the 2022 E3 ACC model.
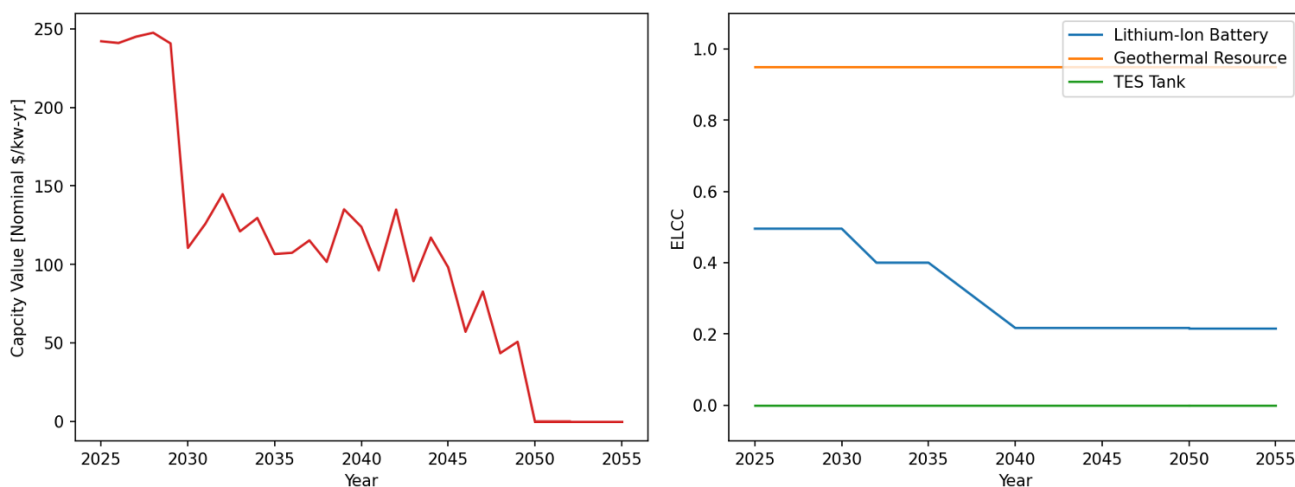
Figure 5: Annual capacity value (left) and battery ELCC (right) forecasts based on the 2022 E3 ACC model.

In the 2022 E3 ACC models, Lithium-ion battery is characterized with 20 years lifetime and 84% roundtrip efficiency. Figure 6 shows forecasts for battery capital expenditure which is calculated based on its energy and power components, where each is associated with a corresponding cost. Additionally, interconnection cost is included to account for connecting the added battery power capacity to the electricity grid. We observe that battery capital expenditure is forecasted to drop significantly, which is closely aligned with recent battery cost projections published by NREL (Cole et al. 2021). Furthermore, we also consider annual fixed costs for maintenance in addition to replacement and augmentation costs which account for maintaining the battery to run with the same efficiency throughout its lifetime. Figure 7 provides a simplified comparison of capacity revenue and battery capital and operational expenditure, and how much net income from the energy market, including both RT and REC, is required to break even across. This analysis is expressed in nominal USD per MWh installed; hence, it is independent of battery power capacity installed. Capacity revenue per MWh and required overall net income are both inversely proportional to battery duration. They are dominated by power capacity in ranges of low battery durations and dominated by energy capacity in ranges of higher battery durations. Eventually, the required overall net income converges to the energy cost for each corresponding year while the capacity revenue per MWh converges to zero with sufficiently large battery duration designs. With these observations, we can analyze the net income required from the energy market, including both RT and REC prices. In this setting, the reader may assume that the battery is a standalone unit that follows near optimal daily arbitrage trades where it is charged and discharged during the lowest and highest prices hours, respectively, every day. In years as early as 2025, a battery unit with less than about 3-hours in duration already records positive annual cashflow even without potential profits from energy markets. However, in later years, the required daily arbitrage margin grows significantly to infeasible magnitudes over years as the capacity value approaches zero and decreases at rates faster than the decrease in battery power and energy costs. Meanwhile, with significantly large durations, the required energy market net income also approaches the energy capacity cost for the corresponding year given the negligible capacity revenue per MWh installed of battery energy capacity.
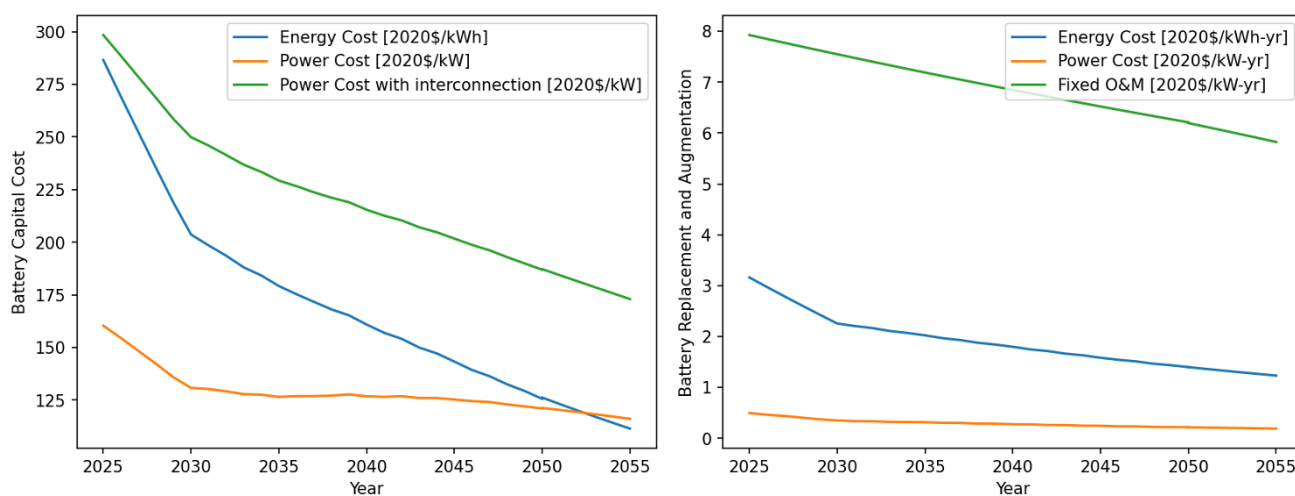

Figure 6: Annual battery power and energy capital costs including interconnection (left), and replacement and augmentation forecast (right).
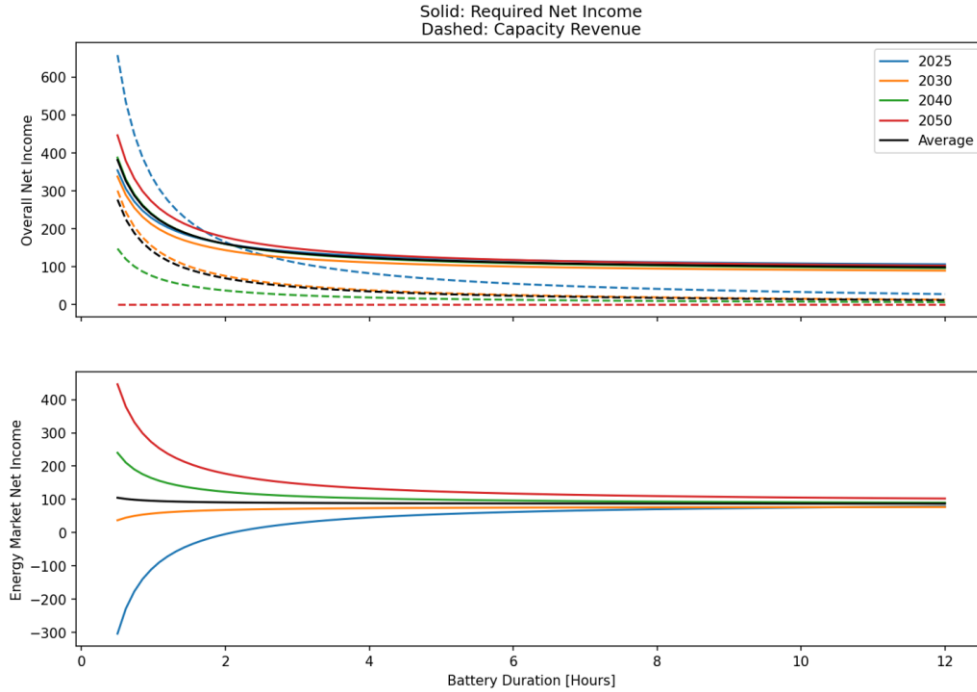
Figure 7: Analysis of how much net income in nominal USD per MWh installed of Lithium-ion battery is required from the energy market, including both RT and REC prices, for an investment in battery power capacity to break even. This is shown for different duration designs and annual forecasts of capacity value and battery capital and operational expenditure.

Additionally, we retrieved the 2021 weather conditions around the California Bay Area and assumed this weather repeats annually for the project lifetime. Particularly, ambient temperature is important as an input into the power plant module which determines the efficiency of converting thermal energy to electricity. Also, we considered other technical and financial parameters which are needed to complete this setup. We considered a subsurface geothermal system with reservoir true vertical depth of 4 km, surface temperature of $20°\,C$, and geothermal gradient of $50\ °C/km$; hence, an initial reservoir temperature of $T_0^r = 220°\,C$. The resource was developed with six producers and six injectors with steady-state producer wellhead mass flow rate of $\dot{m}_t^{prd} = 100\ kg/s$ and capacity factor $CF = 95\%$. Financially, we considered inflated nominal discount rate of 11%, ITC of 30% and no PTC, upstream $OPEX$ of 4 $MM/year, 2% $OPEX$ annual escalation, power plant $CAPEX$ of 2250 $/kW, power plant interconnection cost of 260 $/kW, and TES tank $CAPEX$ of 1435 $/m^3$ (E3 2022; Orsini et al. 2021; Beckers and McCabe 2019).

If operated in baseload mode with no storage facilities, then PPC is the only decision variable which is optimal at 66 MW, which yields $LCOE$ of 51.4 $/MWh. Table 1 shows NPV and equivalent PPA price for various optimized system configurations. An optimal baseload design with 66 MW PPC yields 189.2 $MM, equivalently 82.4 $/MWh PPA, which is higher than the historical average PPA price of around 70 $/MWh. This result indicates that a baseload geothermal developer in California could profit more from participating in the free market rather than seeking and signing an average PPA. The flexible bypass configuration does not require optimization as it is set up such that the operator controls the geofluid to bypass the power plant only when $p_t^{RT} < -p_t^{REC}$. These scenarios are infrequent in the considered forecasts; hence, we only see marginal improvement in NPV to 190.7 $MM, equivalently 82.7 $/MWh PPA. Nevertheless, the capability to bypass could prevent losses in markets with more negative pricing and/or settings with frequent contingent curtailment requirements due to system operational issues, e.g., transmission line congestion.

Table 1: Optimal NPV in $MM for baseload and flexible generation systems compared to typical PPA contract prices. Additionally, we show the equivalent fixed PPA price in $/MWh that would need to be signed to achieve an equivalent NPV.

Configuration	Baseload 66 MW PPC	Flexible Bypass	Flexible Bypass + TES	Flexible Bypass + Battery
NPV ($MM)	189.2	190.7	190.7	309
Equivalent PPA Price [$/MWh]	82.4	82.7	82.7	105

Next, we maintained the option to bypass and introduced storage facilities: TES tank and Lithium-ion battery storage independently. In the case of bypass and TES configuration, the optimizer converged to discarding TES and simply operating as it would with a flexible bypass configuration, again equivalently yielding 82.7 $/MWh PPA. TES tanks are less favorable because they still require excess turbine capacity to convert their thermal energy content into usable power. While the power plant could be oversized to allow for dispatching the TES tank content during on-peak hours, the optimizer found this design choice to be suboptimal. Furthermore, TES tanks do not earn capacity value. Rather, TES tanks are anticipated to hold significant value for flexible geothermal generation in direct-use applications, e.g., district heating. In the configuration of bypass and Lithium-ion battery storage, the optimizer arrived at an optimal design that is significantly superior to other configurations with 309 $MM NPV, equivalently 105 $/MWh PPA. Particularly, the optimizer exploits the considerably high battery capacity value in the first few years as well as the arbitrage opportunity in energy markets. The optimizer chose to reduce the power plant nameplate capacity to 64 MW, and only install a single battery, spanning 2025-2045, with 1-hour duration and 1424 MW power capacity. The 1-hour duration design is demonstrated in Figure 7 while the high power capacity is aimed for the arbitrage opportunity, seen in Figure 4 as the difference between off-peak and on-peak energy prices, which the optimizer converged to as we selectively assume unconstrained demand in both the energy and capacity markets. While we could have constrained demand, this would require a detailed investigation of the forecasted market dynamics

We performed further analysis to understand the techno-economics and rationale behind the optimal decision vector for TES and Lithium-ion battery configurations. While it is a valid objective, *NPV* alone as a quantity does not provide information on the required upfront investment. Rather, a developer is interested in the *NPV* versus *CAPEX* Pareto front to learn how much capital needs to be raised for an anticipated net income. This curve is generated automatically as part of our optimization setup as we already treat this problem as a dual-objective optimization, where we optimize over *NPV* and *Net Income*. Additionally, the optimizer of choice R-NSGA-II makes use of the Pareto fronts as one ranking criterion to elect surviving candidates in the genetic offspring process. Figure 9 show the Pareto fronts generated for the configurations of bypass and battery (top), and bypass and TES (bottom). We provide two views of each: zoomed out (left) and zoomed in (right). With Lithium-ion battery storage, the first few optimization iterations are associated with highly negative NPV due to installing high battery capacities with poor dispatch schedule. Meanwhile, the Pareto front is evident in the zoomed-in plots where the optimizer tends to elect and mutate candidates falling on the Pareto front. These plots also show fewer capital-intensive candidates that fall on the Pareto front, despite having smaller *NPV* as a tradeoff. Meanwhile, the TES configuration falls on a single front, representing the Pareto front because it is constrained by the capacity of the turbine.
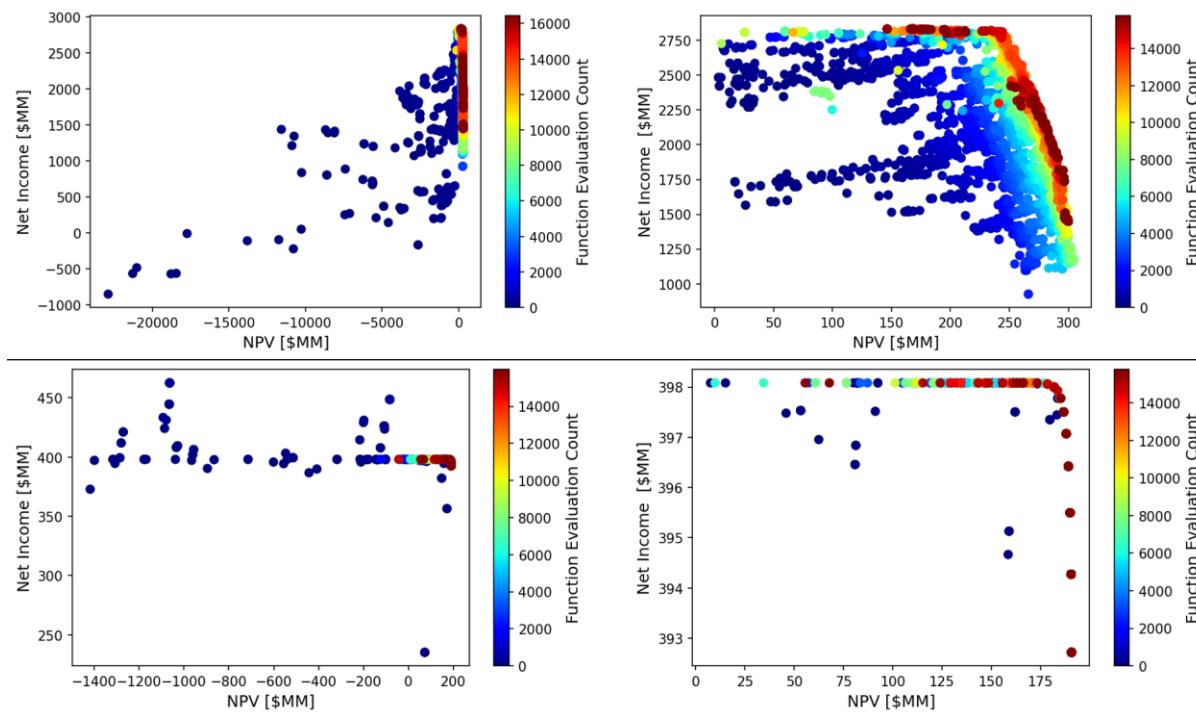

Figure 8: Pareto front of NPV versus Net Income (i.e., optimization objective quantities) for different candidate decision vector in the R-NSGA-II optimization sessions. Top and bottom rows represent the configurations of bypass and battery, and bypass and TES, respectively. Left and right columns represent zoomed out and zoomed in plots, respectively. Each candidate point is colored based on when it was evaluated during the optimization process.
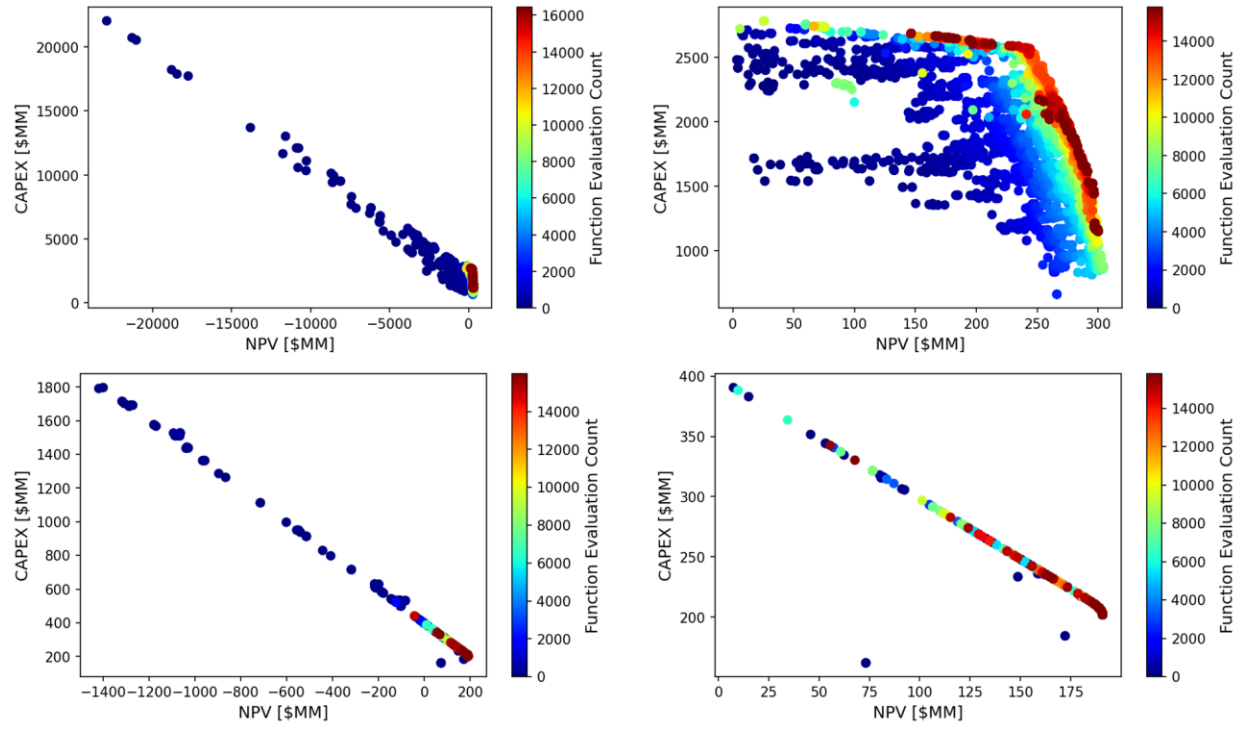
Figure 9: Pareto front converted to a plot of NPV versus CAPEX for different candidate decision vector in the R-NSGA-II optimization sessions. Top and bottom rows represent the configurations of bypass and battery, and bypass and TES, respectively. Left and right columns represent zoomed out and zoomed in plots, respectively. Each candidate point is colored based on when it was evaluated during the optimization process.

We also looked deeper into the configuration of bypass and Lithium-ion battery and visualized the system operations hourly. As seen in Figure 10-11, we show two weeks selected in the first and last years of operations, 2025 and 2054, respectively, to demonstrate various system behaviors. Figure 10 shows the year 2025 where we have a Lithium-ion battery installed. The optimized schedule depicts arbitrage opportunity trading behavior where the battery is charged and discharged during the lowest and highest LMP, respectively, almost daily. We also note that the chosen battery energy capacity 1424 MWh is optimally exploited by the dispatch where SOC spans 0-100% without signs of under- or over-sized battery energy capacity. Furthermore, we note how cumulative capacity revenue (area under the curve) is significantly greater than wholesale RT and RECs market revenues during the year 2025 because of the high capacity price forecasts shown in Figure 5. Toward the end of project lifetime, Figure 11 shows how the system is operating with no battery storage capacity as the optimizer elected to only install a single battery unit whose 20-year lifetime ends by 2045. This choice is justified by zero capacity value during these years of the forecast. Hence, the total power output in this case is simply that of the power plant. We can observe that the optimizer chooses to bypass in cases where $p_t^{RT} < -p_t^{REC}$. Also, we note that the system output is capped just below 40 MW (only 62.5% of the installed 64 MW PPC), which depicts reservoir depletion over time. Additionally, the system power output oscillates between day and night hours because of the oscillating ambient temperature which affects the power plant efficiency.

Figure 10: Hourly operational details of the bypass and battery configuration for a selected week in 2025. From top to bottom, these seven subplots show (1) market prices, (2) ambient temperature, (3) power sold to the market as generated directly from either turbine and battery, (4) geofluid mass flow rates segmentation as either used to generate power sold to the market directly (M_Market), used to generate power used to charge the battery (M_Battery), or bypassed to reinjection (M_Bypass), (5) battery charge and discharge rates, (6) battery SOC, and (7) revenue from wholesale RT, RECS, and capacity markets.
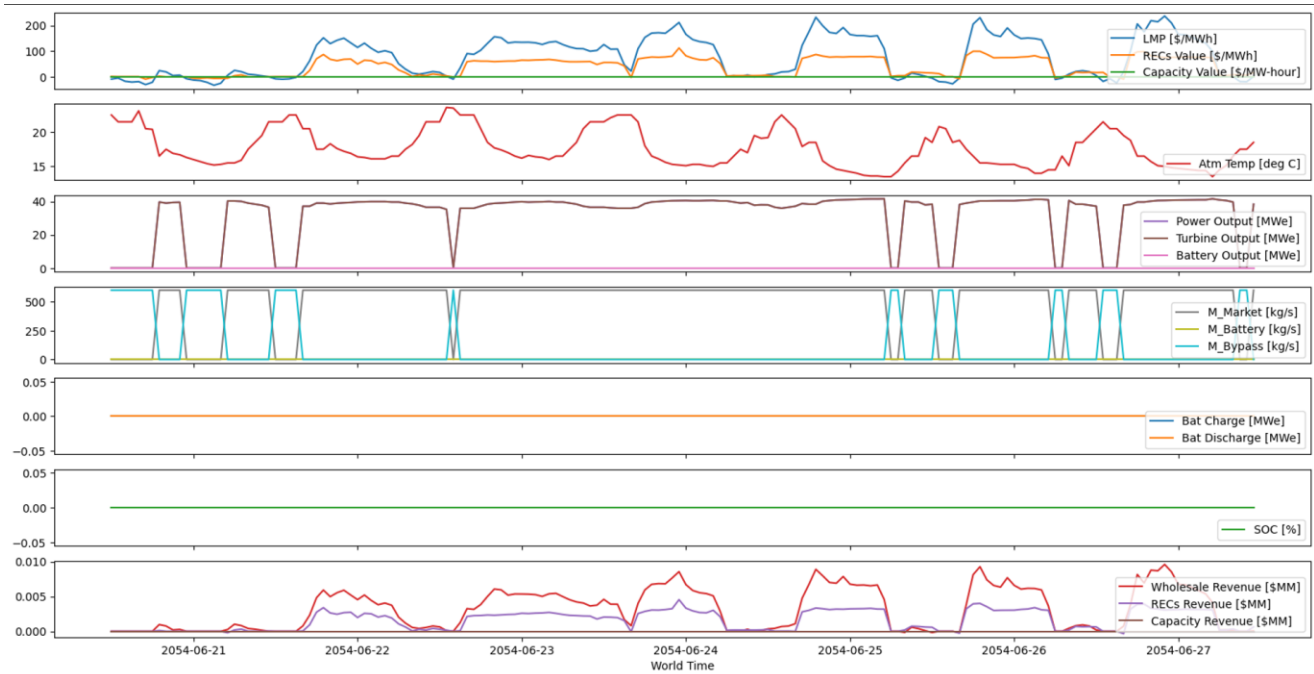

Figure 11: Hourly operational details of the bypass and battery configuration for a selected week in 2054. From top to bottom, these seven subplots show (1) market prices, (2) ambient temperature, (3) power sold to the market as generated directly from either turbine and battery, (4) geofluid mass flow rates segmentation as either used to generate power sold to the market directly (M_Market), used to generate power used to charge the battery (M_Battery), or bypassed to reinjection (M_Bypass), (5) battery charge and discharge rates, (6) battery SOC, and (7) revenue from wholesale RT, RECS, and capacity markets.

3. CONCLUSIONS

In this work, we investigated the techno-economic viability of dispatching geothermal resources directly to the California power market in trading hub NP15, in the absence of a fixed-price PPA. We also investigated the techno-economic viability of flexible geothermal dispatch through means of turbine bypass, TES tank, and Lithium-ion battery storage. Economics was based on the 2022 E3 ACC model forecast of the wholesale RT, capacity, and REC markets. Results indicate that an optimal design with baseload dispatch to the free-market yields NPV equivalent to operating under an 82.4 \$/MWh PPA. Meanwhile, incorporating Lithium-ion battery storage and switching to an optimized flexible dispatch was found to yield significant improvements in NPV, equivalent to operating under a 105 \$/MWh PPA. This demonstrates the potential of geothermal energy to profit from the free market, with enhanced profits if operated flexibly by the developer/operator. Flexible operations are also much needed in decarbonized grids that are largely penetrated by intermittent renewable resources, such as the California electricity grid.

4. LIMITATIONS AND FUTURE WORK

We adopted a simplified conceptual geothermal reservoir model which could be, without loss of computational efficiency, substituted with a more involved analytical model. On the power market side, we used the 2022 E3 ACC forecasts to estimate the energy, renewable, and capacity values of the proposed flexible geothermal system. However, taking full revenue from these forecasts assumes market dynamics where net-positive power generators like the proposed system are uncommon. Additionally, using deterministic forecasts does not capture the uncertainty underlying market revenues, which stems from market price and bidding process uncertainties. Future work could incorporate a power market simulator to forecast multiple potential realizations and capture the uncertainty underlying the profitability of the proposed system.

ACKNOWLEDGEMENTS

REFERENCES

C. Augustine, J. Ho, and N. Blair. Geovision analysis supporting task force report: Electric sector potential to penetration. Technical report, National Renewable Energy Lab (NREL), Golden, CO, 2019.

E3. Avoided Cost Calculator. E3. Retrieved December 21, 2023, from https://www.ethree.com/public_proceedings/energy-efficiency-calculator/. 2022.

K. Beckers and K. McCabe. GEOPHIRES v2. 0: updated geothermal techno-economic simulation tool. Geothermal Energy, 7(1):1–28, 2019.

T. Bergman, Theodore Bergman, Frank Incropera, et al. Fundamentals of heat and mass transfer. John Wiley & Sons, 2011.

J. Blank and K. Deb. Pymoo: Multi-objective optimization in python. IEEE Access, 8, 89497-89509, 2020.

W. Cole, W. Frazier, and C. Augustine. Cost Projections for Utility-Scale Battery Storage: 2021 Update. National Renewable Energy Laboratory (NREL). 2021.

K. Deb and J. Sundar. Reference point based multi-objective optimization using evolutionary algorithms. In Proceedings of the 8th annual conference on Genetic and evolutionary *computation* (pp. 635-642), 2006.

R. DiPippo. Geothermal power plants: principles, applications, case studies and environmental impact. Butterworth-Heinemann, 2012.

P. Dobson, D. Dwivedi, D. Millstein, et al. Analysis of curtailment at the geysers geothermal field, California. Geothermics, 87:101871, 2020.

T. Garabetian. Flexibility services and capacity availability: Towards a business model and regulatory framework for geothermal orc plant market uptake. In Proceedings of the 6th International Seminar on ORC Power Systems, 2021.

B. Garbow. Minpack-1, subroutine library for nonlinear equation system. 1984.

TWI. Geosmart: Towards flexible and efficient geothermal systems, 2020.

F. Hardarson, B. Heimisson, S. Geirsson, et al. Theistareykir geothermal power plant, challenges in a weak electrical grid. GRC Transactions, 42, 2018.

M. Holmgren. X steam for MATLAB. www. x-eng. com, accessed October, 21:2006, 2006.

D. Laszuk. Python implementation of Empirical Mode Decomposition algorithm. GitHub Repository. 2017.

I. Lienhard and H. John. A heat transfer textbook. phlogiston press, 2005.

V. Linga. Most US utility-scale geothermal power plants built since 2000 are binary-cycle plants. 2019.

J. Long, E. Baik, J. Jenkins, et al. Clean firm power is the key to California's carbon-free energy future. Issues in Science and Technology, 2021.

Z. Michalewicz and D. Fogel. How to solve it: modern heuristics. Springer Science & Business Media. 2013.

A. Minson, J. Kivell and T. Fry. Tongonan I geothermal power development, Philippines. Geothermics, 14(2-3):353–370, 1985.

M. Mitchell. An introduction to genetic algorithms. MIT press, 1998.

J. Nordquist, T. Buckanan and M. Kaleikini. Automatic generation control and ancillary services. GRC Transactions, Las Vegas, NV, Sept 2013.

P. Olasolo, M. Juarez, M. Morales, et al. Enhanced geothermal systems (EGS): A review. Renewable and Sustainable Energy Reviews, 56:133–144, 2016.

R. Orsini, P. Brodrick, A. Brandt, et al. Computational optimization of solar thermal generation with energy storage. Sustainable Energy Technologies and Assessments, 47:101342, 2021.

A. Petursdottir, A. Massey, E. Desjardins, et al. Assessing geothermal projects using envision, GRC Transactions, Davis, CA, 2020.

W. Ricks, J. Norbeck, and J. Jenkins. The value of in-reservoir energy storage for flexible dispatch of geothermal power. Applied Energy, 313:118807, 2022.

J. Robins, A. Kolker, F. Flores-Espino, et al. 2021 US geothermal power production and district heating market report. Technical report, National Renewable Energy Lab (NREL), Golden, CO, 2021.

J. Rutqvist, L. Pan, N. Spycher, et al. Coupled processes analysis of flexible geothermal production from steam-and liquid-dominated systems: impacts on wells. In Proceedings, 45th Workshop on Geothermal Reservoir Engineering, Stanford University, Stanford. CA, SGP-TR-216, page 17, 2020.

P. Virtanen, R. Gommers, T. Oliphant, et al. Scipy 1.0: fundamental algorithms for scientific computing in python. Nature methods, 17(3):261–272, 2020.